Fridge Magnets

THESIS

submitted in partial fulfillment of the
requirements for the degree of

MASTER OF SCIENCE
in
PHYSICS

Author :	Freek Hoekstra
Student ID :	—
Supervisor :	Prof.dr.ir. Tjerk Oosterkamp
2nd corrector :	Dr. Wolfgang Löffler

Leiden, The Netherlands, December 21, 2018

Fridge Magnets

Freek Hoekstra

Huygens-Kamerlingh Onnes Laboratory, Leiden University
P.O. Box 9500, 2300 RA Leiden, The Netherlands

December 21, 2018

Abstract

A common problem in Magnetic Resonance Force Microscopy (MRFM) is the spin-induced damping of the cantilever, which drastically limits the sensitivity to spin signals. In order to solve this problem, we have developed improvements to a Persistent Current Switch (PCS) that make it less dissipative and capable of creating a stronger magnetic field at the sample. On top of this, the low noise level that our detection setup requires is conserved. The improvements are based on the use of a low-temperature magnetic core material called MetGlas [1]. We have measured the full B-H curve of the MetGlas and verified that it decreases the current required to switch a Niobium wire to the resistive state by a factor of 30. Furthermore, we have used this data to calculate the performance of a transformer made using this material, and we have calculated the expected extremely low noise level that this circuit will cause in our SQUID.

Contents

Version of December 21, 2018– Created December 21, 2018 - 15:20

Acknowledgements

I want to thank Charlotte for her love and support.

Many thanks also to Tjerk, Martin, and Gesa for the many interesting and sometimes funny conversations we had in the lab, as well as Tom, Thom, Guido and Ruben. Furthermore, I must credit Kier Heeck for suggesting to use a magnetic material despite the reservations our group had: it was his idea that sparked this thesis. Thanks also to Merlijn, as well as Gert, Ko, Bert and Raymond for technical support. Credit goes to Casper Zee for the schemes in Figures 2.5 and 3.1, and for showing the rest of the lab how to do schemes properly. Thanks to fellow Meethallers Tobias, Vera, Wim & Wim for fruitful discussions.

Chapter 1

Introduction to Magnetic Resonance Force Microscopy

Magnetic Resonance Force Microscopy (MRFM) works similarly to conventional Magnetic Resonance methods such as Nuclear Magnetic Resonace (NMR) and Magnetic Resonance Imaging (MRI): a B_0 static field is applied, and a weaker, radio frequency oscillating B_1 field is added perpendicularly to drive the spins in the sample at their resonance frequency. The difference is that in MRFM, a very soft and sensitive cantilever with a magnetic tip is used as a force sensor, as opposed to the inductance-based magnetometers used in NMR and MRI [2] [3].

This enables an improvement in volume sensitivity of a factor 10^6: whereas MRI is limited to resolutions on the order of a few $(\mu m)^3$, MRFM has been demonstrated to reach a few $(nm)^3$ [3] [4].

Conventional scanning probe microscopy techniques like Atomic Force Microscopy (AFM) and Scanning Tunnelling Microscopy (STM) can only measure at the surface of a sample. MRFM however, enables spin imaging at the surface and up to a few microns beyond. MRFM is one of only 2 techniques that enables measurement of spin-relaxation times in 3D with a volume resolution of a few nanometres, along with Nitrogen Vacancy (NV) magnetometry.

There is a number of potential applications. The first and originally intended application of MRFM is 3D non-destructive imaging of biological samples [2] [5] [6].

It also has potential in the study of condensed matter physics. For example, edge states of topological insulators could be studied by locally probing the spin-lattice relaxation time [7].

The state of the art MRFM setups are limited in resolution by the thermal motion of their cantilevers. They typically suffer from cantilever heating caused by the laser that is used to measure the cantilever motion.

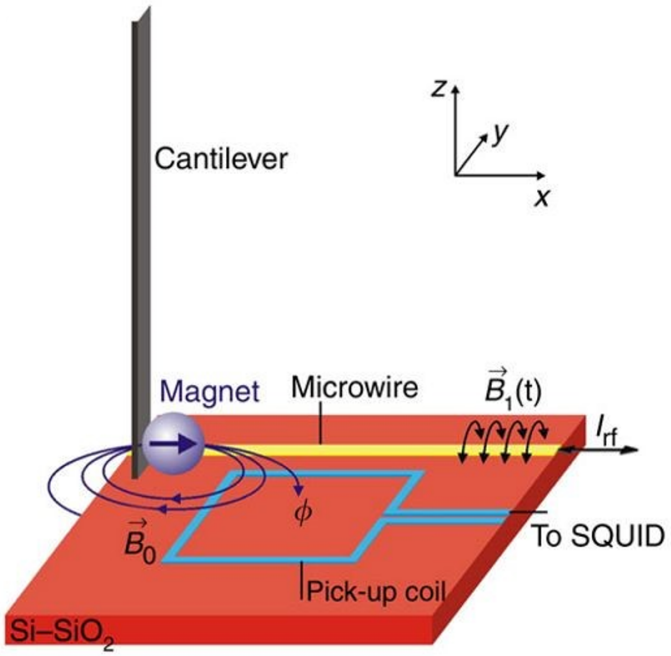

Figure 1.1: *Diagram of the milliKelvin MRFM setup: a cantilever with a fixed magnet attached to the tip, a microwire that is used to apply an RF frequency signal, and a pickup loop for the SQUID that measures the magnetic field change caused by the cantilever movement. Figure from [8].*

This is why our group has chosen to do MRFM at ultra-low temperatures down to 20 mK, using a dry dilution refrigerator. In order to avoid the heating that a laser causes, we measure the cantilever motion by measuring the magnetic flux caused by the cantilever tip using a SQUID. The SQUID has an enormous sensitivity on the order of $10^{-6}\Phi_0/\sqrt{Hz}$. This sensitivity allows us to measure the extremely small variation in flux caused by (typically) 0.1 nm movements of our 3 μm diameter magnetic tip. However, it also means we are very sensitive to any kind of magnetic noise: we are so sensitive that even the flux noise caused by the flipping of ferromagnetic domains inside the screws of our setup can be relevant.

One of the technical limitations of our setup is that the cantilever motion is significantly dampened by interaction with the surface electron spins. The electron spins are coupled to the cantilever through magnetic forces, and they dissipate their energy, and the cantilever's energy, to the lattice. This causes our sensitivity to drop at distances of 1 μm and less between the surface and the magnetic tip. We will investigate this coupling, and introduce a way to address this challenge in Chapter 2. The next Chapters (3 & 4) investigate different parts of the proposed solution and in Chapter 5 we show that the proposed solution is expected to have a sufficiently low

noise level. In order to understand the structure of this thesis, it is highly recommended to read Chapter 2 first.

Chapter 2

How to fix the spoiling influence of the spin bath

Our cantilever force sensor becomes less sensitive near a surface due to unpolarized electron spins on the surface and their coupling to the cantilever. In this chapter, we summarize why this happens and show how a homogeneous magnetic field would reduce this spin dissipation. We also describe the setup we intend to use to solve this problem, and in doing so reveal the structure of the rest of this thesis.

2.1 An intuitive explanation

The cantilever's Q-factor and internal dissipation in vacuum are practically constant in temperature below 1 K. However, when we approach the surface with our cantilever, we observe a decline in Q-factor and an increase in dissipation, especially at smaller tip-sample distances below 1 μm and at lower temperatures. This is detrimental to our signal-to-noise ratio, as we typically have the best performance in this very same regime. This effect was more pronounced at larger distances when we were using bigger tip magnets.

The reason for this collapse of our resonator's Q-factor is the coupling to (mostly) electron spins at the surface. These spins are coupled to the cantilever by magnetic forces: that is the same mechanism we use to measure (nuclear) spin signal. However, the spins are also coupled to the lattice vibrations. These T_1 mechanisms cause a dissipation of spin energy, and thus also of the energy of our resonator.

This effect can be mitigated by applying a homogeneous B_0-field to the entire experiment, increasing the polarization of the spins. A spin ensemble that is more polarized will be less prone to fluctuate, and thus to dissipate,

as we know from the fluctuation-dissipation theorem.

It is easiest to visualize this for an electron spin for which $\mu_{el}B \approx k_B T$, i.e they are on the edge of being polarized or not polarized. A swinging movement of the cantilever will cause the value of B at the electron's position to oscillate. When the cantilever swings close, B and the polarization will increase, and when the cantilever swings away, the polarization will decrease. In the interval when B is weaker, the electron spin will relax and dissipate its energy to the lattice, causing the cantilever to lose energy when it swings back.

The above is an intuitive explanation of how an external field suppresses spin-induced dissipation. A rigorous mathematical analysis is given in section 2.2.

2.2 The spoiling influence of the spin bath

A formalism was developed by Marc de Voogd [9] [10] to calculate the interaction of the cantilever with the electron spins on the sample. He calculates the coupling of a spin to a mechanical oscillator (the cantilever) with a magnetic tip. This coupling results in a frequency shift. The spin dissipates through spin-lattice coupling, leading to a dissipation of the cantilever motion and a lowering of the Q-factor.

The coupling factor in units of inductance is given in equations 2.1 - 2.4.

Spin-cantilever coupling factor in units of inductance	κ
Magnetic moment of surface spin	μ_s
Coldness	$\beta = \frac{1}{k_B T}$
Magnetic flux density (static)	B, B_0
Spatial derivative of B along $\hat{\vec{u}}$	$\vec{B}'_{\parallel \hat{\vec{u}}}$
Second spatial derivative of B along $\hat{\vec{u}}$	$\vec{B}'_{\parallel \hat{\vec{u}}}$
Unit imaginary number	i
Angular frequency in radians per second	ω
Spin-lattice relaxation time	T_1
Spin-spin relaxation time	T_2
Surface spin density	σ
Resonance frequency of cantilever (vacuum)	f, f_0
Cantilever stiffness in vacuum	k_0
Frequency shift of cantilever due to spin coupling	Δf
Cantilever Q-factor	$Q = \frac{\text{resonator energy}}{\text{power loss}}$

Version of December 21, 2018– Created December 21, 2018 - 15:20

$$\kappa_1 = \mu_s \tanh(\beta\mu_s B_0) \cdot |\overrightarrow{B}''_{\parallel \hat{\overrightarrow{B}}_0}| \tag{2.1}$$

$$\kappa_2 = \frac{\mu_s}{B_0} \frac{\beta\mu_s B_0}{\cosh^2(\beta\mu_s B_0)} \cdot |\overrightarrow{B}'_{\parallel \hat{\overrightarrow{B}}_0}|^2 \cdot \frac{1}{1+i\omega T_1} \tag{2.2}$$

$$\kappa_3 = \frac{\mu_s}{B_0} \tanh(\beta\mu_s B_0) \cdot |\overrightarrow{B}'_{\perp \hat{\overrightarrow{B}}_0}|^2 \cdot \left((1 - \frac{2\frac{T_2}{T_1} - (\omega T_2)^2 + i\omega T_2(1+\frac{T_2}{T_1})}{(1+i\omega T_2)^2 + (\omega_s T_2)^2} \right) \tag{2.3}$$

$$\kappa = \kappa_1 + \kappa_2 + \kappa_3 \tag{2.4}$$

The magnetic field caused by the tip is calculated for each position, and then the frequency shift and dissipation are calculated by integrating the coupling over all surface spins.

$$\frac{\Delta f}{f_0} = \frac{C}{2} \cdot \frac{(2\pi f_0 T_1)^2}{1 + (2\pi f_0 T_1)^2} \tag{2.5}$$

$$\Delta\frac{1}{Q} = C \cdot \frac{(2\pi f_0 T_1)^2}{1 + (2\pi f_0 T_1)^2} \tag{2.6}$$

$$C = \frac{\sigma\mu_s}{k_0} \int\int \kappa dA \tag{2.7}$$

This theory can be used to fit the spin density to a measurement of the cantilever motion near the surface [11].

It is straightforward to add a homogeneous external magnetic field to these calculations and numerically evaluate the resulting dissipation and Q-factor.

2.3 How much B_0 field do we need?

It has previously been shown [12] that any applied external magnetic field in MRFM must be parallel to the magnetization of the cantilever tip magnet. Any applied field that is more than a few degrees off will cause significant twisting of the cantilever tip, thereby drastically reducing its sensitivity as a force sensor. In our case, the magnetization direction of the tip is fixed to be parallel to the surface of the sample, since the RF-frequency B_1 field is applied via a microwire on-chip, thus perpendicular to the surface, and the static B_0 field must be perpendicular to the B_1 field.

An external magnetic field that is parallel to the tip magnetization is anti-parallel to the B_0 field caused by the tip at the location of the sample. Thus we expect that non-zero, small values of B_{ext} locally reduce the value of $|B_0|$ and increase spin coupling in certain parts of (T, z) parameter space.

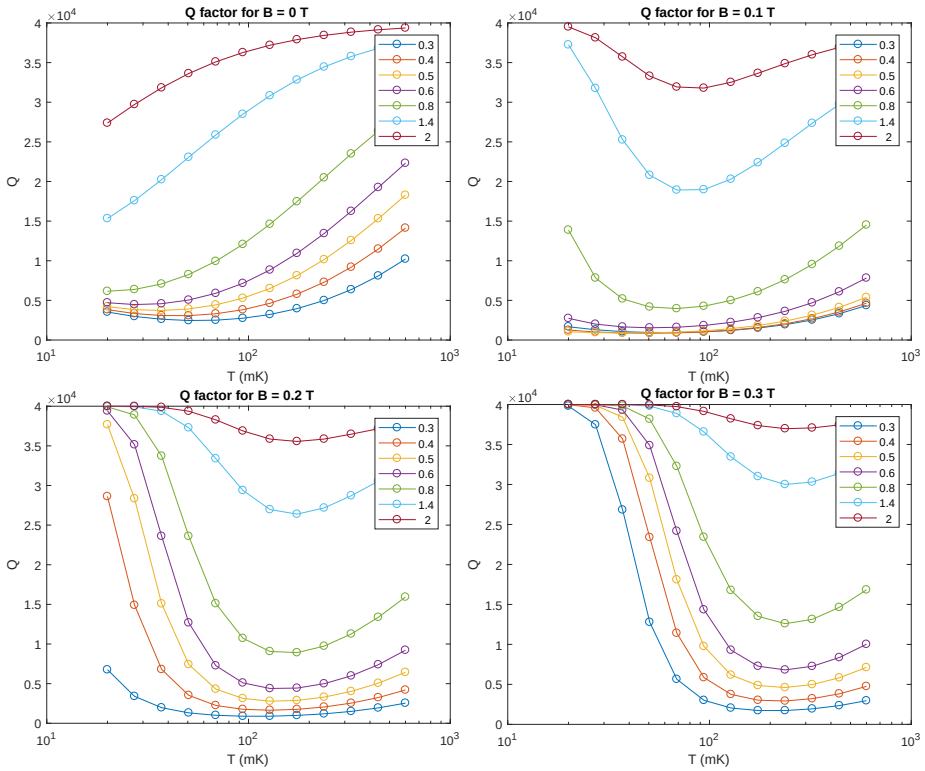

Figure 2.1: *Calculations of the spin-induced cantilever dissipation. The vertical axis is the Q-factor of the cantilever, the horizontal axis is the sample temperature. The different lines are for different tip-sample distances, which are indicated in* μm *on the inset of each figure. The different figures are calculated for different values of the external magnetic field.*

This undesired effect can be overcome by applying a stronger magnetic field, as can be seen in Figures 2.1 and 2.2.

From Figures 2.1 and 2.2, we conclude that an external magnetic field will reduce the spin contribution to Q-factor damping, for values of the external magnetic field greater than 200 mT at temperatures below approximately 40 mK. Thus we decide to aim for a design flux density of 300 mT: this will significantly reduce spin damping with some margin.

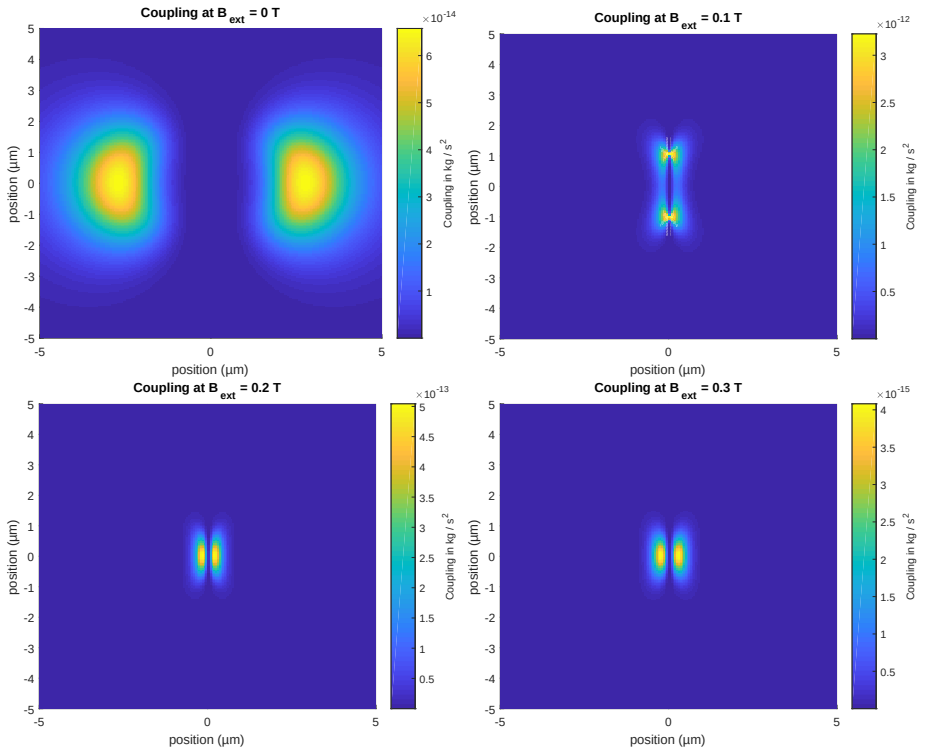

Figure 2.2: *Calculations of the spin coupling C per spin according to equation 2.7 for 0.6 µm between the tip and the sample, at 30mK. The x and y axis are the position on the sample surface, the color indicates the strength of the coupling.*

2.4 How do we do this?

To generate these fields we have previously [12] made a split air coil (see Figure 2.3) which can generate a reasonably homogeneous magnetic field with a strength of 85 mT/A at its center.

Because of the SQUID detection we need this field to be extremely low in noise. Directly applying a current source to superconducting coils at the experiment is not a feasible option, because of the noise level. A good current source may reach a noise level of 0.1 mA. Estimating that we require a total flux density on the order of 0.3 T, and we expose a pickup loop area on the order of $(10^{-4}\text{m})^2$ that gives us a flux noise of the order of $10^5 - 10^6$ Φ_0, which is about 11 orders of magnitude too high: our SQUID noise floor is around $10^{-5} - 10^{-6}$ Φ_0.

Thus we decide to use a Persistent Current Switch, drawing on earlier experience of the group with this kind of circuit [12] [13]. In this setup (see Figure 2.4), a superconducting switch effectively short circuits the coil. When the field in the coil needs to be changed, the shortcut should be driven from the superconducting to the normal state.

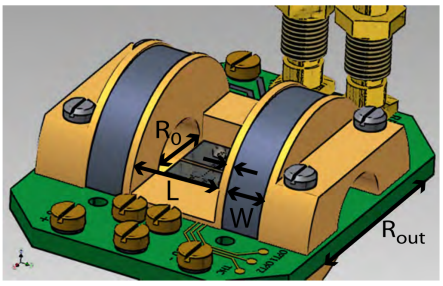

Figure 2.3: *Picture of the coils from [12]. The field strength at the center is 0.085 T/A and the inside diameter of the coils is around 9 mm. For further details, see [12].*

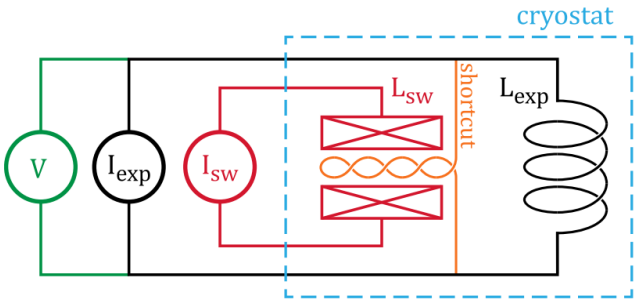

Figure 2.4: *The black circuit drives a current through a coil L_{exp}. The superconducting shortcut, in the form of a twisted Nb wire, can be switched to its normal state using the switching coil L_{sw}. The voltage across this parallel LR circuit is measured by a voltmeter, to measure the response during charge and discharge. The components within the blue dashed lines are at low temperature inside the cryostat, where the connecting wires are superconducting. Figure from [13].*

Our focus will be on the use of a ferromagnetic material, in order to:

1. increase the current we can insert into the superconducting loop with a transformer.
2. decrease the current required to switch to the normal state.
3. have zero current through the switch when it is in its normal state, i.e. no Joule heating during switching.

The operation of this new circuit, as depicted in Figure 2.5, would be as follows:

1. Turn on* I_{sw} to bring the short to the normal state, thereby uniting the 2 superconducting loops into a single superconducting loop.
2. Turn on* I_1 to induce an equal current through L_2 and L_{exp}, let's call these currents I_2 and I_{exp}. The current through the short is the difference $I_2 - I_{exp}$

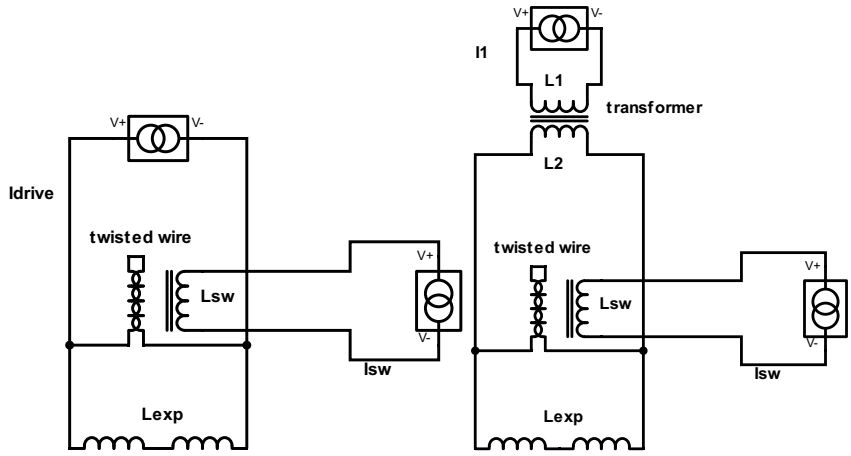

Figure 2.5: *Left: the 'classic' Persistent Current Switch circuit based on [13], with only 1 improvement: the switching coil uses a MetGlas core (as in Chapter 3). During charging of the superconducting loop, there is a non-zero current through the resistive short, causing heating. Right: Our design. Because of flux conservation in a superconducting loop, we can charge L_exp with no current through the short, and thus no dissipation.*

3. Turn off* I_{sw} to let the short go back to the superconducting state, thereby splitting the superconducting circuit into 2 superconducting loops.

4. Turn off* I_1 and disconnect the current sources to minimize the noise in L_{exp}.

The result of this sequence of operations is a persistent current I_{exp} running only in the loop through L_{exp} and the short.

In this thesis, we assess the performance of such a circuit in the following chapters: we study the magnetic properties of a Metal Glass, a ferromagnetic material for transformer cores at 4.2K in Chapter 3, we calculate the expected performance of a transformer with such a core in Chapter 4 and then we calculate the expected noise performance of our circuit in Chapter 5.

* Every change in current should be done with a slow ramp to reduce eddy heating and core loss, since both of these dissipative processes scale with $|\frac{dI}{dt}|$.

Chapter 3

The magnetic properties of Metal Glass at 4.2 K

In this chapter we investigate a magnetic material that may help us to generate the magnetic fields called for in Chapter 2 in a practical way. We demonstrate a persistent current switch that can be switched with a current well below 100 mA. Also we calculate that the material studied may be used as core material for a superconducting transformer to increase the current in the field-generating coils.

In order to create high currents in a superconducting circuit without high Joule heating in connectors, a transformer can be used to drive a high current through the experiment while only sending a low current through the connectors. Although air transformers can be made, they are much less efficient than designs with a magnetic core. We also require a high flux density to operate our magnetic superconducting switch. Using a high permeability magnetic material will drastically decrease the current required to create this flux.

The only materials with very high magnetic permeability at low temperature are amorphous alloys or so-called 'metal glasses'. This is because they have very small magnetic domains, which are less likely to freeze at low temperatures. Changing the magnetic field inside a material with this property leads to very small dissipation because its magnetization curve has very little hysteresis, which makes it suitable for our application. In this chapter, we measure the magnetization curve of the material by winding a superconducting coil around it and measuring the voltage across the coil with a 4-point measurement. This curve can be used to calculate the properties of a transformer. By also inserting a Nb wire between the 2 halves of our core, we have effectively made a magnetic superconducting switch.

Earlier research [14] has shown that MetGlas type 2714A has a relative permeability in excess of 10^4 at low temperatures. In this chapter, we test

cut cores from the same manufacturer, made of MetGlas 2605SA1, since 2714A cores are not available in the size and shape (C cut) that we need.

3.1 Setup

We wound a superconducting coil of 1600 turns around one half of a AMCC-1SX amorphous alloy (Metal Glass) C-cut core [1] and measured the voltage over the coil during a voltage (current) ramp. The wire used for the coil is Supercon TB48-M 127 μm insulated wire with a Cu matrix and a single 62 μm NbTi filament inside. Between the 2 halves of the C-cut core, we put a 50 μm insulated Nb wire, to test whether this superconducting wire can be switched to the normal state; the results of this experiment are in section 3.4. The whole setup is taped with Teflon tape to a copper extension on a dipstick, and is submerged in liquid Helium so it is cooled to a temperature of 4.2 K.

A photo and schematic drawing of the setup can be found in Figure 3.1. We facilitate a low-temperature 4-point measurement on a component by spot welding 2 NbTi wires to each end of the component on a Nb foil. The foils of both ends of the wire/coil are then wrapped in white Teflon tape in such a way that they are isolated. This procedure was done for both the coil and the Nb wire. Details of the spot welding procedure can be found in [13]. Thus, one 4-point measurement leads to one package of Nb foil electrically insulated in Teflon tape, with 2 wires protruding from one side, and 4 wires going up from the other side. Two such packages can be seen in the photo in Figure 3.1. Relevant geometric quantities and other constants that are used in the calculations of this chapter can be found in Table 3.1.

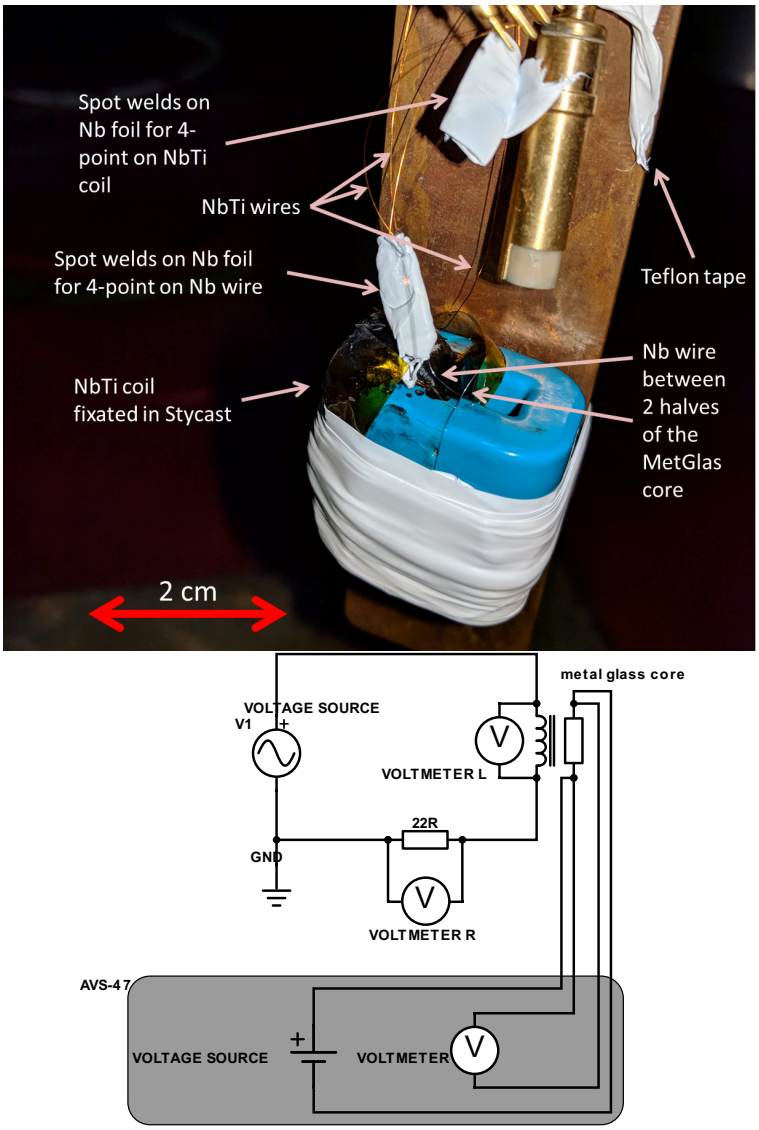

Figure 3.1: *Top: a picture of the experiment at the tip of our dipstick. Bottom: The full schematic of the experiment. In the top-right of the experiment, we see the coil wrapped around the Metal Glass core, with a Nb wire between the halves, indicated as a resistor coupled to the core. This part, as well as all its 4-point connections, is at 4.2K, while the rest of the setup, including the 22 Ω resistor, is at room temperature. The depiction of the AVS-47 is heavily abstracted.*

Table 3.1: ** estimated, ** extracted from AMCC datasheet [1]*

Turns	N	1600
Parallel resistor	R	22Ω
Magnetic length of the core	l_{mag}	66 mm **
Cross-section area of the core	A	150 mm^2 **
Air gap		$0.05 - 0.15mm$ *
Core weight (includes both halves)		60 g

A voltage was applied to the coil and series resistor in a triangular waveform, using a voltage buffer capable of 0.6 A at 10 V. Due to the changing inductance L of the coil when near saturation, the use of a current source was not possible: the feedback electronics of two of our current sources both started to oscillate when trying to drive into saturation.

3.2 Data analysis

We measured the voltage over the coil and the resistor for a number of periods, then averaged over all periods to get a single "waveform" with voltages v_L and v_R defined during the 10 second period with a sampling rate of 1 k Sa/s. From this we calculated the current I and inductance $L(I)$ using equations 3.1 - 3.3.

$$I = \frac{v_R}{R} \tag{3.1}$$

$$v_L = \frac{d\Phi}{dt} = \frac{d}{dt} B \cdot A \tag{3.2}$$

$$L(I) = \frac{v_L(I)}{dI/dt} \tag{3.3}$$

The current can easily be converted to an applied field H or magnetomotive force (MMF) F through equations 3.4 and 3.5.

$$H = \frac{N \cdot I}{l_{mag}} \tag{3.4}$$

$$F = N \cdot I \tag{3.5}$$

We then use this inductance to calculate the magnetic permeability $\mu(H)$ of the material using equation 3.6, which is integrated to calculate the magnetic flux density $B(H)$ (equation 3.7). This is equivalent to a time integral of $\frac{v_L}{A}$, as can be deducted from equation 3.2.

$$\mu(H) = L(H) \cdot \frac{l_{mag}}{AN^2} \tag{3.6}$$

$$B(H) = \int_0^H \mu(H')dH' = \int_0^{t_H} \frac{v_L(t)}{A} \tag{3.7}$$

where t_H denotes the time at which a certain applied field H is reached.

3.3 Results

3.3.1 Magnetization curve

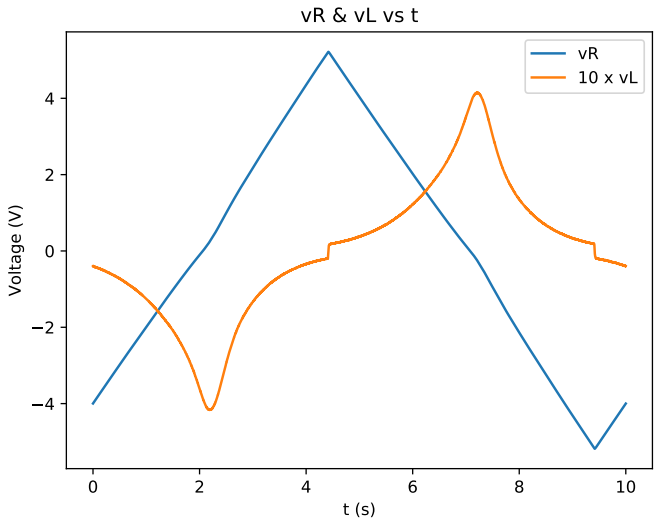

Figure 3.2: *The voltage over the superconducting coil vL and the power resistor vR, averaged over 40 periods. Data from a measurement in which we applied a triangular waveform with an amplitude of 6V and a frequency of 0.1 Hz. Note that the voltage over the coil vL has been multiplied by 10 for reasons of clarity.*

The 'raw' data, averaged over multiple periods, is plotted in Figure 3.2. By applying equations 3.1 - 3.7, we can calculate the full magnetization curve from these 2 voltages, which is the result we have plotted in Figure 3.3. Furthermore, we can calculate the expected dissipation in the cores, which is very important, not only because heating can break superconductivity and cause quenching of our switch coil; we also need to limit heating in our dry dilution refrigerator during MRFM experiments. This calculation is performed in section 3.3.2.

Figure 3.3 shows that the flux density at an MMF of 380 Ampère-turns (A·turns) is calculated to be 1.4 T. This is in good agreement with the saturation field of 1.56 T given by the manufacturer. Recall that the MMF is

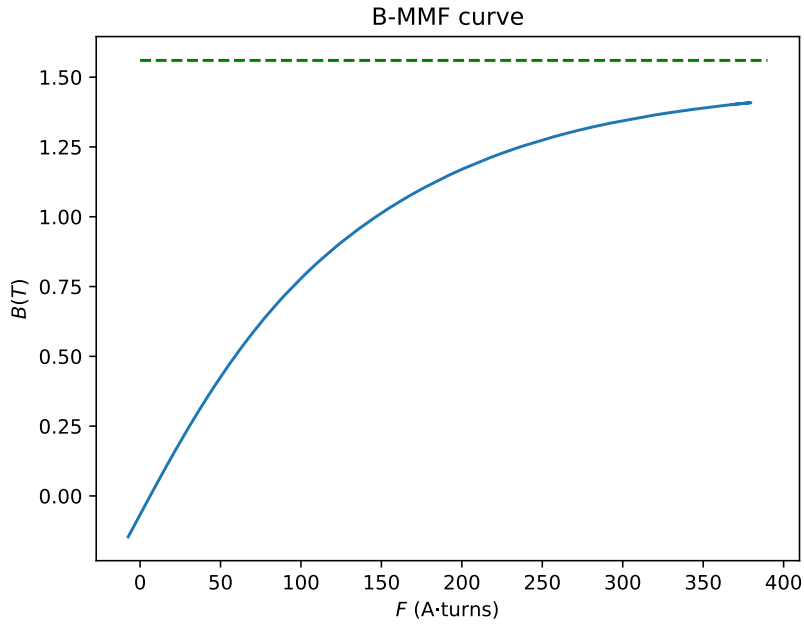

Figure 3.3: *A calculated $B - F$ curve in blue, from a measurement in which we applied a a triangular waveform with an amplitude of 6V and a frequency of 0.1 Hz. In green the saturation field of 1.56 T, as provided by the manufacturer. $F = \int Hdl = N \cdot I$, this is a useful quantity to determine the required number of turns and current, and only differs from H by the magnetic length, which we do not know very precisely.*

$F = \int Hdl = N \cdot I$: this is a useful quantity to determine the required number of turns and current for a specific flux density. It only differs from H by a factor magnetic length, which we do not know very precisely and depends only on the geometry of our core.

A linear fit to the region below 80 A·turns shows that the relative permeability of this specific core, with the small air gap, is approximately 600. This corresponds to the theoretical maximum for a core with a magnetic length l_{mag} on the order of 60 mm and an air gap of 0.1 mm: $60/0.1 = 600$. This suggests that a transformer with no intentional air gap can saturate at even lower MMF.

3.3.2 Dissipation

What is the dissipation in the cores?

In Figure 3.4, we extrapolate the room temperature dissipation log-log plot provided by the manufacturer and estimate a dissipation of roughly 3 mW/kg at 0.1Hz. This puts the dissipative power at around 200 µW. For a

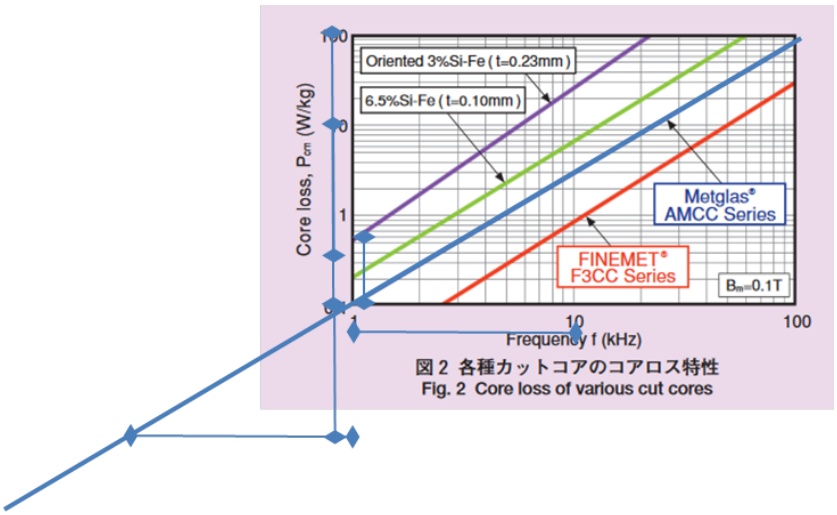

Figure 3.4: *A rough graphical extrapolation of the log-log dissipation graph provided by the manufacturer [1] tells us that the dissipation is about one and a half order of magnitude below 0.1W/kg, the lowest tick on the vertical axis, at 3 mW/kg at 0.1 Hz.*

ramp up and down time of 5 seconds (half the period), this leads to a dissipation of 1 mJ, and an energy per unit volume of 100 Jm^{-3}, approximating the density of iron as 8 g cm^{-3}.

As can be seen in Figure 3.6, there is an exponential decay at the moment in time when our driving current is at the peak of the triangular waveform, see Figure 3.2. Since this happens at the point where $|I|$ is at a maximum, this will impact the shape of our $B - F$ curve at the edges, and not the center of the hysteresis loop. This is why, instead of naively calculating the area between the back and forth parts of our magnetization curve, we instead look at the gap in H around $B = 0$, and approximate the inherent dissipative area as a triangle: $\frac{E}{V} = \frac{1}{2} B_{triangle} H_{gap}$.

From Figure 3.5, we estimate a H_{gap} of 6 A·turns, and a $B_{triangle}$ of 0.7 T. This leads to a dissipation energy per unit volume of 30 Jm^{-3}, which is a factor 3 lower than the value obtained from the graphical extrapolation of the room temperature specifications.

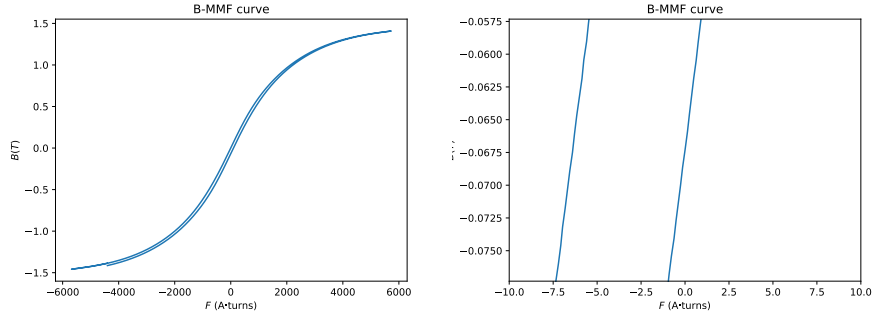

Figure 3.5: *Left: The B-F curve, right: zooming in shows a gap of 6 A·turns.*

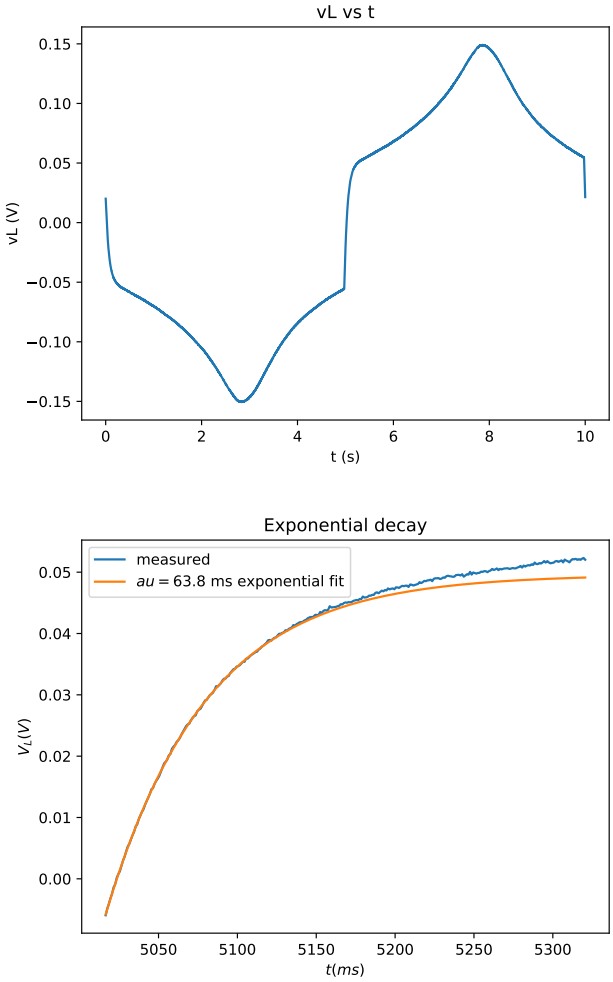

Figure 3.6: *This figure is based on data of a 2Vpp measurement: 3 times lower maximum current than for the other figures in this chapter. Top: $v_L(t)$; bottom: A zoomed in view of the graph just after the 5 second mark. A fit to the exponential decay of $v_L(t)$ shows that it is of the order of the LC-frequency $\frac{1.5H}{22\Omega} \approx 68$ ms, taking into account the fact that the inductance is reduced by saturation (the inductance scales linearly with v_L). An artefact like this will contribute to the area of the magnetization curve, and thus to a calculation which overestimates the actual hysteresis. This happens at the point in time where the sign of v_L (see Figure 3.2) and thus of dI/dt, changes. At this point, $|I|$ is at a maximum: thus we are at the edges of the $B-H$ curve, and not in the center of the hysteresis loop.*

3.4 Switching experiment

We now use the setup described in section 3.1 to measure the resistance of the 50 µm Nb wire as a function of the current through the superconducting coil. To do this, we use a Picowatts AVS-47 resistance bridge to measure the resistance of the Nb wire using a 4-point measurement.

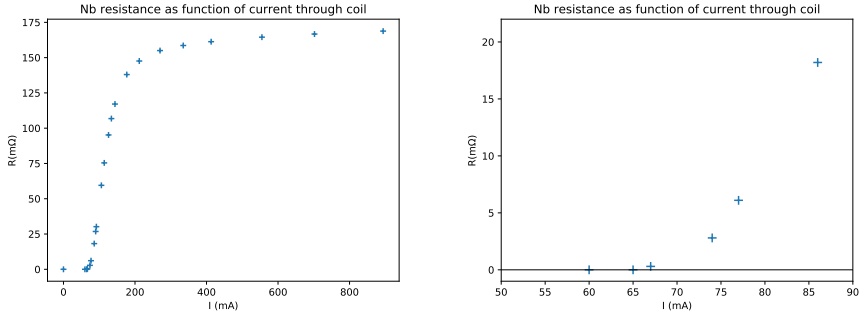

Figure 3.7: *Left: The resistance of the Nb wire as a function of the current through the magnet coil, right: zoomed in on the transition, with a black line through zero resistance.*

The data in Figure 3.7 shows that we switch at 66 mA through the 1600 turns, which corresponds to an MMF of 105 A·turns and, according to the data in Figure 3.3, leads to a flux density of 810 mT in the core. An air-coil based magnetic superconducting switch with the same Nb wire switched at approximately 600 mT of field [13]. This difference can easily be attributed to a small field leakage or a widening of the effective area inside the air gap of our core, as compared to the field within the core itself, as well as the uncertainty in the effective area of our magnetic circuit.

3.5 Conclusion

We have measured that Metal Glass cut cores have a high permeability $\mu_r >$ 600 and low core loss $<$ 3 mW/kg at 4.2 K. This means they can be used as transformer cores in the design of a persistent current circuit for B0-field at low temperatures, enabling us to send more current through the magnet coils. However, operation at 10mK still needs to be tested.

On top of this, a magnetic superconducting switch using this material was shown to break superconductivity of a Nb wire with an applied current of only 66 mA. This is about 30 times less current than was used in earlier work [13] with an air coil, while our switching coil had more than 5 times fewer turns and a less optimal geometry for switching: a larger encapsulated volume.

The MetGlas core reduces the stray field, and thereby possible eddy heating of nearby components of the dilution refrigerator, and the lower required current reduces the risk and severity of quenching, as does the lower number of turns of the magnetic switch coil. This combines to make our magnetic switch potentially easier, faster and more reliable to operate in a dilution refrigerator at few milliKelvins.

Chapter 4

A Metal Glass core superconducting DC transformer for B0-field at low temperature

Introduction

In this section, we calculate the properties of a superconducting transformer wrapped around the Metal Glass of which we tested the magnetic properties at 4.2K in Chapter 3. We also fabricate a superconducting transformer around this core and calculate the maximum flux density we can achieve at the experiment when the DC transformer is saturated, and which changes are necessary to reach 300 mT.

4.1 A superconducting DC transformer

A typical transformer takes an alternating current (AC), uses a primary coil L_1 to create a change of flux $\frac{d\Phi}{dt}$, which leads to an induced voltage in a secondary coil L_2. By choosing the inductances and winding numbers of the coils sensibly, this means a low-voltage, high-current signal can be converted, or vice-versa. The magnetic field generated by the coils is typically trapped in a metallic core with high magnetic permeability, to reduce stray field, and thus energy leakage.

Typical transformers only work with AC, not with static currents (DC), because there is no induced voltage when there is no change of flux $\frac{d\Phi}{dt}$. However, the flux inside a superconducting loop is conserved, meaning that an induced flux by a static (DC) current through L_1 will induce a cur-

rent I_2 through L_2, provided that there is a full closed loop of superconducting material to flow through.

Typical transformers are not used in the regime where the fluc density inside the core is so high that it saturates: they are used in the regime where the $B-H$ curve of the core material is still linear, so as not to distort the signal. For our intent however, there is no signal, only a current that we want to set as high as possible. Thus we are going to calculate how the $B-H$ curve of our core material influences the current I_2 through our secondary and experiment coils.

How much current can we generate with the transformer we built? We know that the upper bound for flux through the secondary coil is $\Phi = B_{sat} \cdot N_2 \cdot A$. But choosing N_2 too large will mean a less favourable turns ratio N_2/N_1.

4.2 Theory

Beyond the linear regime, the inductances of coils wrapped around the magnetic material are not constant: we need to use the experimental data of the B-H curve of our magnetic material to optimize our transformer design.

From our previous experiments, we know $B(H)$. There may be some deviation from this curve, as this was measured with the coil wound directly around the core. Our transformer will have at least one of the coils on a coil holder, which creates 1 to 2 mm extra separation between the core and the inner windings of the coil. However, it will also have slightly more windings than the 1600 of the previous one. Overall, this curve will be a good enough approximation.

In a transformer, the H field applied by the primary coil is partially cancelled by the second coil: $H_{tot} \cdot l_{magn} = I_1 \cdot N_1 - I_2 \cdot N_2$. It is evident that it is easier to calculate with the Magnetomotive Force (MMF) in Ampère windings $F_{net} = H \cdot l_{magn}$ instead of the applied field H. We fit a hyperbolic tangent to our measured B-H (or B-F) curve, as can be seen in Figure 4.1. The hyperbolic tangent is the generally accepted model for the initial magnetization curve, as it provides the expected behaviour in small field, as well as both saturation limits. More advanced models that include hysteresis are based on the same tanh lossless model [15][16].

Now we know the total flux through the secondary circuit is still zero.

$$\Phi_2 = B(F_{net}) \cdot N_2 \cdot A - I_2 \cdot L_{exp} = 0 \tag{4.1}$$

with A the area of the transformer core. And from that, we iteratively solve

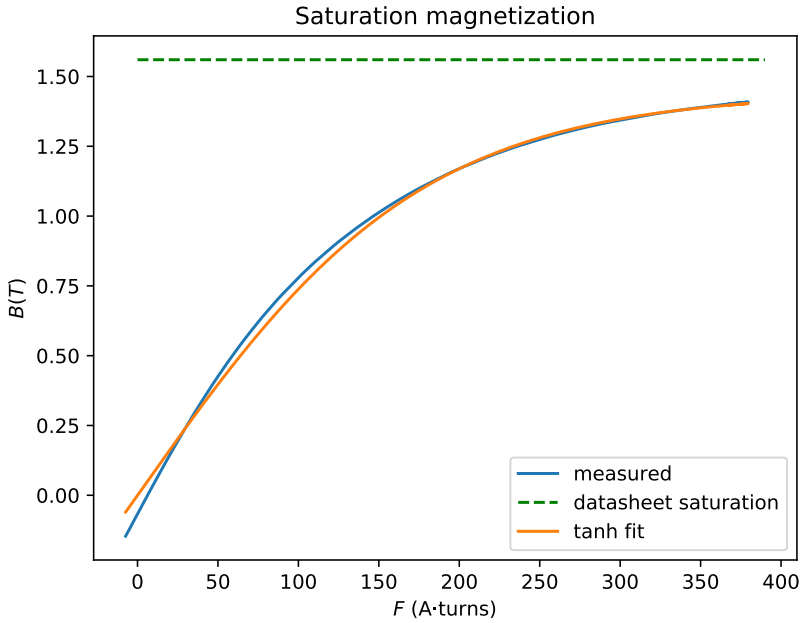

Figure 4.1: *The measured data and the fit. Note that this is a modified B-H curve where the H axis has been replaced by the MMF. This is a more convenient choice for a fixed geometry.*

for the secondary current, starting from $I - 2 = 0$, using:

$$I_2 = \frac{B(F_{net}) \cdot N_2 \cdot A}{L_{exp}} \tag{4.2}$$

$$F_{net} = I_1 \cdot N_1 - I_2 \cdot N_2 \tag{4.3}$$

The results of this calculation are in Figure 4.2. We have calculated I_2 for the geometry of the core we have, with fixed $N_1 = 1700$, as a function of I_1 and N_2.

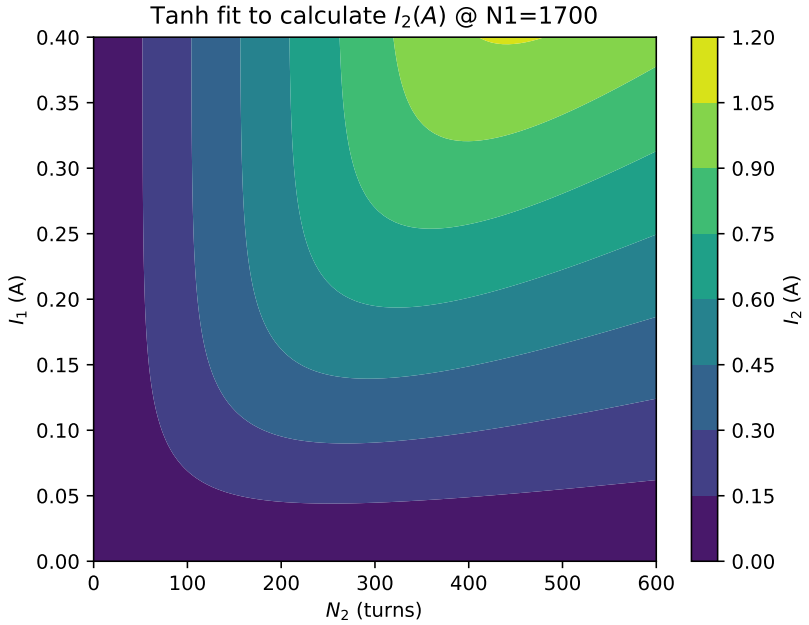

Figure 4.2: *The expected performance of a transformer with 1700 primary coil windings, using the MetGlas core we measured in Chapter 3, and a tanh fit of the B-H curve. We see the saturated behaviour in the top-left: increasing I_1 does not yield an increase in Φ and I_2. We see the negative effect of a lowering turn ratio in the 'linear' regime on the right side: raising N_2 decreases N_2/N_1 and thus decreases I_2. The optimum is in the minima of the contour lines along the center of this figure. A minimum in contour lines is a maximum I_2 for a given I_1, thus optimal current amplification.*

4.3 Conclusion and outlook

Even with only 1700 windings on the primary coil, we can already saturate the magnetic core with an N_2 of 350 at 0.4 A. In order to increase the amount of current in the secondary loop to the required 3.5 A, we need to increase the amount of flux $\Phi = BA$ going through the secondary loop. Since we can apply strong enough fields to saturate the MetGlas, B is fixed so the only the only way to increase the flux is to increase the area: we need a bigger core. Many MetGlas C-cut cores are available from Hitachi Metals [1], all of them bigger in size than the ones we have tested here. We will also need more windings on the primary coil to saturate a core with a larger effective area, but mostly the reluctance will go up, since it scales with the magnetic length. Luckily, most cores have a higher $\frac{A_{eff}}{l_{mag}}$ than the ones we tested [1].

Chapter 5

Noise calculations

In this chapter we calculate the expected noise level in our SQUID due to the improved Persistent Current Switch.

Being able to send more current into a Persistent Current Switch is not useful if it negates the primary advantage of a PCS: low noise levels. There are two aspects of MetGlas that make us wary of noise levels: the high magnetic permeability for small applied fields increases the flux noise caused by current noise through a coil, and the ferromagnetic domains inside the material itself may randomly (thermally) flip, causing additional flux noise.

The SQUID's noise floor is around $10^{-5} - 10^{-6}\Phi_0/\sqrt{\text{Hz}}$. In this chapter, we calculate how the expected induced flux noise due to the PCS compares to that number.

5.1 Noise in I_2

The flux noise induced in the secondary coil will lead to a current through the shortcut, but not through the experiment coils once the shortcut is in the superconducting state and isolates the experiment coils from the transformer (see Figure 2.5 in Chapter 2). The main noise source in our persistent current circuit is the magnetic switch itself: flux noise is induced in the short through current noise in the switch coil $L_s w$ and flux noise in the Metal Glass core.

Table 5.1: *Values of parameters*

Magnetic susceptibility	μ	$600 * 4\pi * 10^{-7}$ H/m
Magnetic length of the core	l_{mag}	$6.6 * 10^{-2}$m
Cross-section area of the experiment coils	$A_{L_{exp}}$	$6.4 * 10^{-7}$m^2
Number of turns of switching coil	N	$1.6 * 10^3$
Flux quantum	Φ_0	$2 * 10^{-15}$ Wb
Effective area of wirebonds to SQUID	A_{SQUID}	10^{-8}m^2
Effective area of short	A_{short}	10^{-6}m^2

5.1.1 Contribution of current noise

For the current noise, we find a value of 0.1 mA RMS between 20 Hz and 10 MHz in the Agilent 6626A datasheet [17]. Since no further information about the noise spectrum is given, and this is a rough estimate, we assume this to be white noise. We then calculate the flux noise that a current I_{sw} through the switching coil causes in our SQUID detector using equations 5.1 and 5.2.

$$\Phi_{short} = \frac{\mu N A_{short}}{l_{mag}} \cdot I_{sw} \tag{5.1}$$

$$\Phi_{SQUID} = 10^{-2} \cdot \frac{A_{SQUID}}{A_{L_{exp}}} \cdot \Phi_{short} \tag{5.2}$$

Equation 5.2 is based on the following reasoning, where we start at the back of the formula and work our way towards the front: all net flux noise that enters into the short Φ_{short}, will cause the same flux noise in the experiment coils. We turn this into a flux density by dividing by the area in the experiment coils $A_{L_{exp}}$. This flux density is then multiplied by the effective area with which the external field couples into the SQUID. Note that this area is much smaller than the area of the pickup loop, as the external field is parallel to the surface in which the pickup loop lies: we expect most of the coupling to be through the wirebonds, which are, in our current setup, exposed to the magnetic field produced by the experiment coils. Finally, the factor 10^{-2} is the order of magnitude of the coupling from the SQUID's input coil to the SQUID itself, based on SQUID sensor datasheet (not publicly available).

We estimate an effective area of the imperfectly twisted wire on the order of 1 mm^2, which is on the large side. We use $\mu_r = 600$ for the relative permeability, which is derived from the data in Chapter 3. Estimating an effective coupling area to the SQUID (through loops of wirebonds mainly) on the order of $(0.1 \text{ mm})^2$, we arrive at a rough estimate on the order of:

$$\Phi^{SQUID} \approx 3 \cdot 10^{-4} \Phi_0 / \sqrt{\text{Hz}}$$

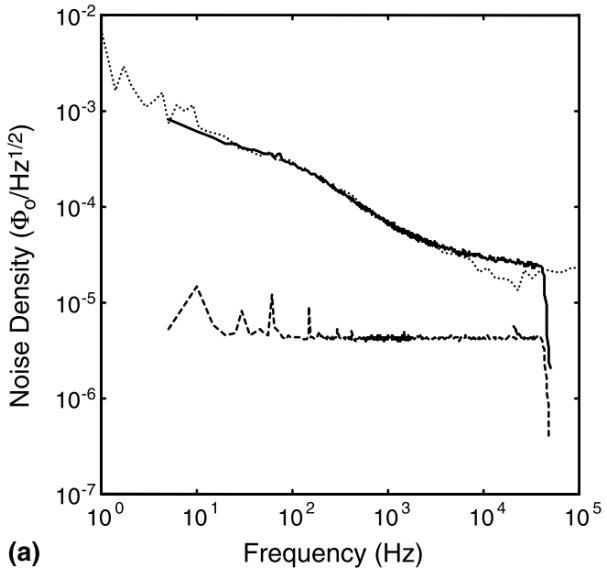

Figure 5.1: *The noise spectrum of MetGlas2714A from [14] at 4.2K. The solid line is the measurement, the dotted line a calculation based on the transfer function and the fluctuation-dissipation theorem. The dashed line is the SQUID noise floor.*

This is still too high, however we can simply detach the current source when we have achieved a persistent current.

5.1.2 Flux noise in MetGlas

Area of AMCC core	$A_{AMCC-core}$	$1.5 * 10^{-4}\text{m}^2$
Area of MetGlas 2714 core from [14]	$A_{2714-core}$	$7.3 * 10^{-6}\text{m}^2$

A second source of noise in the magnetic switch is the magnetic flux noise of the MetGlas itself. We will calculate the contribution of this noise using the data from [14], measured on MetGlas 2714A, a slightly different variant of MetGlas than the material we use.

In the paper, they measured the flux noise in a loop with an area of 7.3 $(\text{mm})^2$. The flux noise spectral density at 3 kHz (our cantilever resonance frequency) is around $10^{-4}\Phi_0/\sqrt{\text{Hz}}$ at 4.2 K, as can be seen in Figure 5.1. This is expected to be lower at our much lower operating temperatures, however for the sake of being conservative, we will use this number in our estimations.

We assume that the flux noise from the different domains is uncorrelated and that the number of domains influencing the noise scales with the area of the (cut) core. Thus the variance scales with the area, and the RMS of the average flux density noise scales with the square root of the area of the loop.

$$\begin{aligned}\Phi_{short} &= B_{2714} \cdot \sqrt{\frac{A_{AMCC-core}}{A_{2714-core}}} \cdot A_{short} \\ &= \frac{\Phi_{2714}}{A_{2714}} \cdot \sqrt{\frac{A_{AMCC-core}}{A_{2714-core}}} \cdot A_{short} \end{aligned} \tag{5.3}$$

Calculating for the area of our cores, 150 $(mm)^2$, using equations 5.3 and 5.2, we find a value for the SQUID noise of:

$$\Phi_{SQUID} \approx 1 \cdot 10^{-8} \Phi_0 / \sqrt{\text{Hz}}$$

5.2 Conclusion

This calculation is not watertight, but it is a result that gives reason to be optimistic, especially considering our conservative parameter estimates. The flux noise appears to be well below (>2 orders of magnitude) the SQUID noise level, and the current noise should not be a problem, as we do not need to have a current source connected during our measurements.

Version of December 21, 2018– Created December 21, 2018 - 15:20

Chapter 6

Conclusion

We have developed and tested a magnetically operated superconducting switch, using MetGlas as a core material, and calculated the expected performance of a transformer based on the same core material. Furthermore we have calculated the expected performance in terms of reduced spin dissipation and expected noise levels.

Our findings indicate that this improved Persistent Current Switch (PCS) circuit allows for more current to be sent through the experiment coils. It enables PCS operation with no dissipation due to Joule heating in the switch, and while needing 30 times less current to operate the magnetic switch. Eddy heating is reduced both because the magnetic core materials create less stray field than the previously used air coil [13], and because there is no need to quickly charge the experiment coils: there is no local Joule heating during operation of the switch, thus all currents can be ramped slowly.

Besides reducing spin-induced dissipation at the lowest temperatures and tip-sample distances by a factor of 3, this method also enables measurements with higher Boltzmann polarization [18] in the MRFM setup, and measuring the size and orientation of the magnetic moment of the tip magnet [12].

In order to reach our goal of 300 mT, we will need to use a larger transformer to increase the flux entering the secondary coil at saturation. Luckily, larger MetGlas cores are readily available [1].

Bibliography

[1] *Amorphous Low Core loss Cut C-Cores https://www.hitachimetals.com/materials-products/amorphous-nanocrystalline/powerlite-c-cores.php*.

[2] J. A. Sidles, *Noninductive detection of single-proton magnetic resonance*, Applied Physics Letters **58**, 2854 (1991).

[3] M. Poggio and B. E. Herzog, *Force-detected Nuclear Magnetic Resonance*, Micro and Nano Scale NMR: Technologies and Systems , 1 (2017).

[4] W. Rose, H. Haas, A. Q. Chen, N. Jeon, L. J. Lauhon, D. G. Cory, and R. Budakian, *High-Resolution Nanoscale Solid-State Nuclear Magnetic Resonance Spectroscopy*, Physical Review X **8**, 011030 (2018).

[5] J. A. Sidles, J. L. Garbini, K. J. Bruland, D. Rugar, O. Züger, S. Hoen, and C. S. Yannoni, *Magnetic resonance force microscopy*, Reviews of Modern Physics **67**, 249 (1995).

[6] C. L. Degen, M. Poggio, H. J. Mamin, C. T. Rettner, and D. Rugar, *Nanoscale magnetic resonance imaging*, Proceedings of the National Academy of Sciences **106**, 1313 (2009).

[7] J. J. T. Wagenaar, *Magnetic Resonance Force Microscopy for Condensed Matter*, PhD thesis, Leiden University, 2017.

[8] A. Vinante, G. Wijts, O. Usenko, L. Schinkelshoek, and T. H. Oosterkamp, *Magnetic resonance force microscopy of paramagnetic electron spins at millikelvin temperatures*, Nature Communications **2**, 572 (2011).

[9] J. M. De Voogd, J. J. T. Wagenaar, and T. H. Oosterkamp, *Dissipation and resonance frequency shift of a resonator magnetically coupled to a semi-classical spin*, Scientific Reports **7**, 42239 (2017).

[10] J. De Voogd, *Magnetic Resonance Force Microscopy and the spin bath : towards single-spin massive-resonator entanglement and the spoiling influence of the spin bath*, PhD thesis, Leiden University, 2018.

[11] M. de Wit, G. Welker, M. de Voogd, and T. Oosterkamp, *Density and T1 of surface and bulk spins in diamond in high magnetic field gradients*, (2018).

[12] J. J. T. Wagenaar, *Magnetic Force Microscopy of paramagnetic electron spins in the presence of an external magnetic field, MSc thesis*, 2013.

[13] B. van Waarde, O. Benningshof, and T. Oosterkamp, *A magnetic persistent current switch at milliKelvin temperatures*, Cryogenics **78**, 74 (2016).

[14] H. P. Quach and T. C. P. Chui, *Low temperature magnetic properties of Metglas 2714A and its potential use as core material for EMI filters*, Cryogenics **47**, 279 (2004).

[15] K. Z. Sokalski, *An approach to modeling and scaling of hysteresis in magnetic materials. Magnetization curve*, Acta Physica Polonica A **127**, 850 (2015).

[16] J. Takács, *A phenomenological mathematical model of hysteresis*, COMPEL - The international journal for computation and mathematics in electrical and electronic engineering **20**, 1002 (2001).

[17] *Agilent 6626A Datasheet www.agilent.com/find/6620*.

[18] M. De Wit, G. Welker, J. J. T. Wagenaar, F. G. Hoekstra, and T. H. Oosterkamp, *Feasibility of imaging using Boltzmann polarization in nuclear Magnetic Resonance Force Microscopy*, arXiv e-prints (2018).